

Effect of the Lattice Crystallinity on the Electron–Phonon Relaxation Rates in Gold Nanoparticles

Wenyu Huang, Wei Qian, and Mostafa A. El-Sayed*

Laser Dynamics Laboratory, School of Chemistry and Biochemistry, Georgia Institute of Technology, Atlanta, Georgia 30332-0400

Yong Ding and Zhong Lin Wang

School of Materials Science and Engineering, Georgia Institute of Technology, Atlanta, Georgia 30332-0245

Received: May 20, 2007; In Final Form: June 13, 2007

In order to study the importance of surface phonons on the electron–phonon relaxation in plasmonic nanoparticles, the effect of size, shape, and materials have recently been studied. Gold and silver nanoparticles have shown no dependence on size and shape while copper nanoparticles have shown some size dependence. This suggests that the bulk phonons, which are sensitive to the bulk-phase structure, are solely responsible for the relaxation of the hot electron in gold and silver plasmonic nanoparticles. The importance of bulk phonons should depend on the degree of crystallinity. In the present study, we have found that the electron–phonon relaxation rate decreases greatly when polycrystalline prismatic gold nanoparticles are annealed and transformed into nearly single-crystalline nanospheres. The results are explained by the presence of high-density grain boundaries with dense, high-frequency molecular type vibrations which are effective in removing the energy of the excited electrons in the polycrystalline prismatic nanoparticles.

I. Introduction

Plasmonic nanoparticles have received great attention because of their novel properties of enhanced near electromagnetic fields, wavelength tunable light absorption and scattering, and strong photothermal effect. These superior properties afford many potential applications of plasmonic nanoparticles in subwavelength optical energy transfer waveguides, biosensors, imaging, and cancer therapy.^{1–8} For all of these applications, it is very important to understand properties of plasmonic nanoparticles, such as laser induced shape transformation,⁹ thermal stability,¹⁰ and electron¹¹ and phonon^{12,13} dynamics. One of the most active research fields is the study of electronic energy relaxation processes of laser excited plasmonic nanoparticles.^{14–18} This is because the electron–phonon interaction is the most important energy relaxation process in materials and determines many important properties, such as thermal conductivity, electrical conductivity, and the nature of superconductivity.¹⁹

The effects of the size and shape of plasmonic nanoparticles on their electron–phonon relaxation dynamics have been studied extensively with the advancement of ultrafast laser spectroscopic techniques, such as time-resolved transmissivity and reflectivity experiments.^{20–28} The relaxation process of ultrafast laser excited coherent electrons starts with the rapid loss of their phases via electron–electron interaction on a time scale of tens of femtoseconds.²⁹ Following the pure dephasing processes, an electron lattice equilibrium state is reached by transferring the electronic energy to the lattice through electron–phonon

interaction on a subpicosecond to several picosecond time scale.³⁰ The energy is finally transferred to the environment by phonon–phonon interaction, which is dependent on the thermal conductivity and heat capacity of the medium and the coupling between the nanoparticle and the surrounding medium.

Quantum-kinetic calculations predict that the electron–phonon relaxation rate increases if the nanoparticle size is decreased below the mean free path of the conductive electrons (40–50 nm in gold) as a result of the interaction between the electrons and the surface phonons. However, experiments by our group and Hartland's group did not experimentally observe such a trend. Within our group, Ahmadi et al.^{21,22} found that for gold nanoparticles of sub-10 and 30 nm there is no difference in the electron–phonon relaxation dynamics. Link et al.³⁰ found that the electron–phonon relaxation time for gold nanoparticles of 9 and 48 nm are very close to each other, approximately 1.6 ps. The shape dependent electronic energy relaxation has also been studied in our group by Link et al.,²³ where they found the electron–phonon relaxation times for gold nanorods (aspect ratio of 3.8) probed at both their longitudinal (750 nm) and their transverse (520 nm) plasmon band are around 3 ps. The same value is also observed in gold nanospheres of 15 and 48 nm.^{15,23} This observation indicates that the changes in the gold nanoparticle's shape, size, and the mode of surface plasmon oscillation do not affect their electronic energy relaxation dynamics.

Hartland's group^{20,24,31} studied silver nanoparticles of 10–50 nm and gold nanoparticles of 4.6–120 nm in aqueous solutions. They found that the electron–phonon coupling constants are very close to each other for nanoparticles of

* Corresponding author. E-mail: mostafa.el-sayed@chemistry.gatech.edu.

different sizes. They also found the coupling constants are similar to the corresponding bulk values.^{24,32} The observed size independence of the electron–phonon relaxation of gold and silver plasmonic nanoparticles is attributed to relatively small contributions of the electron–surface phonon coupling whose coupling constant is known to be proportional to the ratio of the metal atomic valence to its atomic mass (n/m).^{32,33}

For sub-10 nm silver nanoparticles imbedded in a glass matrix, Del Fatti et al.²⁵ and Halte et al.³⁴ found that the rate of electron–phonon relaxation increases with a decrease in the diameter of the nanoparticle. These results were explained by the enhanced interaction between electrons and surface phonons, while the effect of heat transfer to the matrix environment could also play a large role, especially for small nanoparticles that have a high surface-to-volume ratio.³⁴ Darugar et al.³⁵ found size-dependent electronic energy relaxation in spherical copper nanoparticles of 12 and 30 nm. The contribution of surface phonon modes to the total electron–phonon coupling is given by the ratio of the valence of the metal to its atomic mass (n/m).^{32,33} This ratio for copper is twice as large as that for silver and three times as large as that for gold. Therefore, the size dependent electron–phonon relaxation dynamics resulting from the participation of surface phonons in copper nanoparticles is detected more readily than in gold or silver nanoparticles. This can explain why size dependent electron–phonon relaxation dynamics in copper nanoparticles (larger than 10 nm), but not in gold or silver nanoparticles of the same size range, was observed.

From the above, it is clear that most of the electron–phonon relaxation involves bulk phonons. These phonons, however, should be sensitive to whether the particle is in a single-crystalline, polycrystalline, or amorphous state. Most of the lithographically made nanostructures have polycrystalline or amorphous structures because of the nature of the fast rate of atomic deposition. However, upon thermal treatment of these nanoparticles, they can be annealed to form a crystalline nanoparticle.

In the present study, we performed time-resolved transient absorption experiments with different laser pump powers on gold nanoparticles of nearly single-crystalline and polycrystalline internal structures. A simple thermal annealing is used to transform the as-deposited polycrystalline prismatic nanoparticles into nearly single-crystalline spherical nanoparticles. We observed a large difference in the electron–phonon relaxation times for the polycrystalline prismatic and nearly single-crystalline spherical nanoparticle pumped at the same laser pulse energy. The different electron–phonon relaxation dynamics in these two kinds of nanoparticles are attributed to the effect of the internal crystalline structure on the bulk phonon structure. Since polycrystalline prismatic gold nanoparticles have a high density of grain boundaries, which are efficient in inelastic electron scattering, this results in a shorter electron–phonon relaxation time. Another way of saying this is that amorphous or polycrystalline solids have a high density of short wavelength or high-frequency phonons (or even localized molecular type vibrations), which are more efficient in removing high electronic energy resulting in faster electron–phonon relaxation processes.

II. Experimental Section

The nanoparticle is fabricated on a quartz substrate using a modified nanosphere lithographic (NSL) technique.^{36–38} A suspension of highly monodisperse polystyrene (PS) spheres is purchased from Duke Scientific Corp. and used as received. The diameter of the PS spheres used in our experiments is 0.45 μm . Quartz slides (Technical Glass Products, Inc.) are used as

the substrate and are cleaned in piranha solution (H_2SO_4 –30% H_2O_2 , 3:1) at 80 °C for 1.5 h. The quartz slides are placed in a solution of H_2O – NH_4OH –30% H_2O_2 5:1:1 and sonicated for 1 h to render the surface hydrophilic. Circular microscope cover glass pieces (18CIR-2, Fisher Scientific) are treated in the same way as quartz slides and dried in ambient condition. Ten microliters of a mixed solution of the PS sphere suspension and ethanol (1:1) are deposited on a piece of dried circular cover glass. Before the PS sphere suspension fully expanded over the circular cover glass, it is gently dropped on the surface of water. The polystyrene spheres are released from the cover glass and form a close packed uniform monolayer. One drop of 2% dodecylsulfate surfactant is added to water to tune its surface tension, which makes the polystyrene spheres pack tightly. A clean quartz slide is used to pick up the PS sphere monolayer from the water surface. After the evaporation of the water in ambient condition, the PS sphere monolayer crystal forms and covers several square millimeters, up to a square centimeter in area on the substrate. The mask is then mounted in a thermal evaporator (PVD75 Filament Evaporator, Kurt J. Lesker Company), where a layer of gold (99.99%) is deposited onto the PS sphere mask and into the voids between the spheres. The thermal evaporator is equipped with a quartz crystal thickness monitor to control the thickness of the gold deposition layer. After deposition, the PS spheres are removed in a tetrahydrofuran (THF) solution. The prepared prismatic nanoparticle has a bisector of 100 nm and a thickness of 34 nm.

Thermal annealing is performed at 1000 °C for 90 s in a N_2 atmosphere to transform as-deposited polycrystalline nanoprisms into single or nearly single-crystalline nanospheres on a quartz substrate. The gold prismatic or spherical nanoparticle monolayer arrays on quartz substrates are analyzed using scanning electron microscopy (LEO 1530 thermally-assisted field emission SEM, Zeiss/LEO). For the transmission electron microscopy (JEOL 4000EX high-resolution TEM, JEOL Ltd.) measurement, a TEM grid is used to pick up the closely packed polystyrene sphere monolayer from the water surface. The deposition and lift-off processes are kept the same as those performed on a quartz substrate. To protect the carbon film on the TEM grid, the annealing is performed at 771 °C for 15 min in a high vacuum TEM chamber. The absorption spectra of the prismatic and spherical nanoparticle arrays are recorded with a Beckman DU-650 spectrophotometer. The incident light is perpendicular to the array substrate. The transmitted light through the sample has a cross section of several square millimeters.

A femtosecond laser system³⁹ is used to perform the transient absorption experiment. Briefly, a frequency-doubled Nd:vanadate laser (Coherent Verdi) is used as the pump for the Ti:sapphire laser system (Clark MXR CPA 1000). This generates laser pulses of 100 fs duration (full width at half-maximum, fwhm) with energy of 1 mJ at 800 nm and a repetition rate of 1 kHz. A 400 nm pump pulse is generated by frequency doubling of the 800 nm fundamental in a 1 mm β -barium borate (BBO) crystal. The pump beam is mechanically chopped at 500 Hz by a synchronous light beam chopper (HMS 221), which is controlled by a master clock generator (Clark-MXR DT 505). A white-light continuum probe pulse is generated by focusing a small portion ($\sim 40 \mu\text{J}$) of the 800 nm fundamental beam of the Ti:sapphire laser into a 1 mm sapphire plate. The wavelength range of the white-light femtosecond probe pulse is from 400 to 1100 nm. The time delay between the pump and the probe pulses is tuned by a computer controlled optical delay line with a spatial resolution of 3 μm (temporal resolution of 20 fs). The

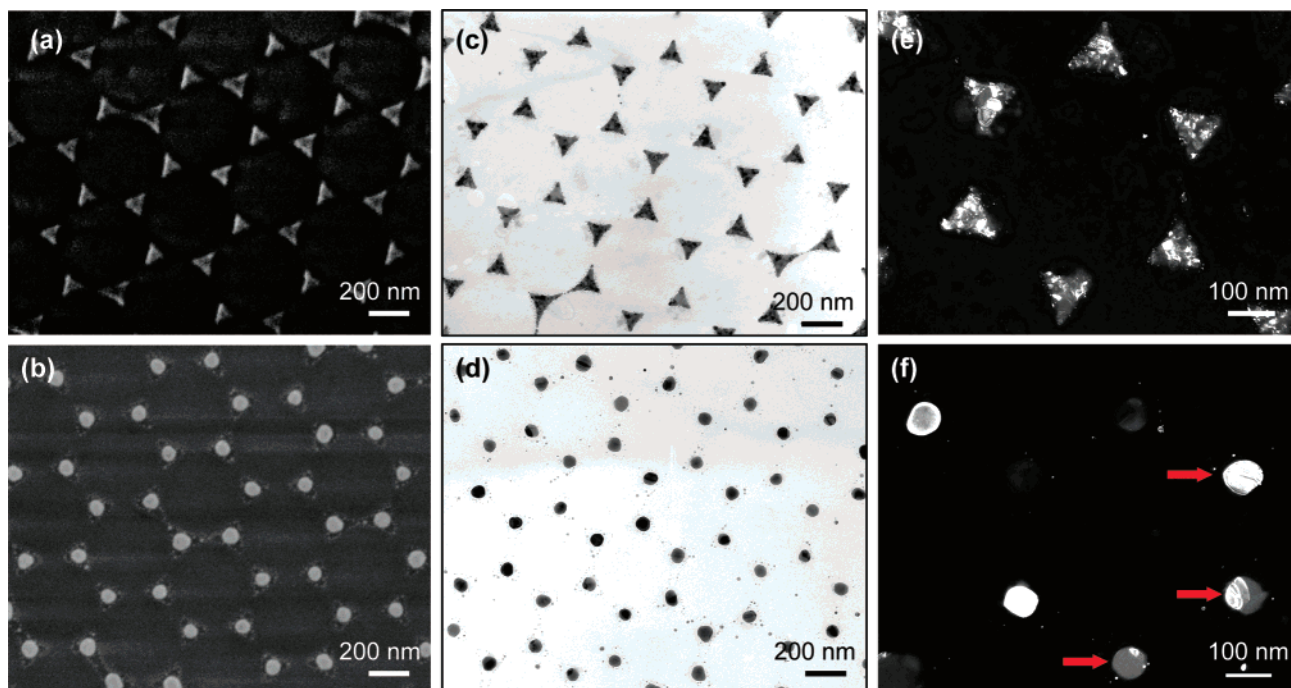


Figure 1. (a and b) SEM images of the gold nanoprism and nanosphere arrays, respectively. The periodic arrays of spherical gold nanoparticles are prepared by thermally annealing the original prismatic gold nanoparticle array samples in an oven at 1000 °C for 90 s. (c) TEM image of the gold nanoprism array. After in situ heating the sample to 771 °C in the TEM chamber, the morphology of gold particles is more like a spherical array (d). The different grain size of gold particles in nanoprism and nanosphere arrays can be identified in their dark-field TEM images (e and f, respectively).

pump and probe laser pulses are focused on the sample with an overlap diameter of 250 μm . The laser pump pulse energy used in our experiment is reduced to less than 300 nJ with neutral density filters. The differential transmission signal $S(t)$ is recorded with a pair of silicon photodiodes (Thorlab) and a lock-in amplifier (Stanford Research Systems). The recorded signal $S(t)$ can be expressed as

$$S(\lambda, t) = \frac{\Delta T}{T} = \frac{I_{\lambda, t} - I_{\lambda, 0}}{I_{\lambda, 0}}$$

where $\Delta T/T$ is the percent change in the transmission of the probe light; $I_{\lambda, t}$ is the intensity of the probe light at wavelength λ after a delay time t from the pump laser pulse, and $I_{\lambda, 0}$ is the intensity of the probe light at λ without the pump. As a result, the recorded signal represents a transient bleach when $S(\lambda, t)$ is larger than zero. The relaxation times of the transient bleach signals were obtained by simulating the experimental data $S(\lambda, t)$ via convoluting the theoretical response function $S(\lambda, t)$ with the instrumental response function $R(t - \tau)$. The detailed description of this approach was reported previously.³⁵

III. Results and Discussion

A. Sample Characterization. Figure 1a is an SEM image of the as-deposited prismatic nanoparticle array on a quartz substrate fabricated with the NSL technique. Since the spherical shape is the most thermodynamically stable, the spherical nanoparticle array on a quartz substrate shown in Figure 1b is prepared by thermal annealing (at 1000 °C for 1.5 min) of the prismatic nanoparticle array shown in Figure 1a. After thermal annealing, the gold nanospheres remain in the same periodic hexagonal arrangement as that of the original prismatic nanoparticles.

To examine the internal crystal structure of the prismatic and spherical nanoparticles with high-resolution transmission elec-

tron microscopy (HRTEM), we fabricated the same sample on TEM grids. Figure 1c is a bright-field TEM image of the as-deposited prismatic nanoparticle array. Even though the thermal annealing temperature of nanoprisms on the TEM grids (771 °C) is lower than that on the quartz substrate (1000 °C), the gold nanoprisms can also be transformed to spherical or nearly spherical nanoparticles (Figure 1d). The nanoprism can be annealed to a spherical shape at a temperature that is much lower than the bulk melting temperature. This is due to the relatively lower melting temperature of the nanoscale material than that of its bulk, which has been observed in nonspherical platinum¹⁰ and silver⁴⁰ nanoparticles. Furthermore, the sharp apexes of silver prismatic nanoparticles can transfer to rounded shape even at room temperature.⁴⁰

Figure 1e is a dark-field TEM image of the as-deposited gold nanoprism, which shows different grain sizes and domains in each nanoprism as indicated by contrast variation. After thermal annealing, the grain size becomes much larger in the spherical nanoparticles as shown in Figure 1f. Because of the difference in the lattice orientations of nanospheres relative to the incident electron beam, some of the spheres can diffract more electrons and thus are shown as brighter spots. Some of the spheres are still not single crystalline as indicated by the differences in the contrast of their dark-field images (marked by red arrows), but the grain size in those nanospheres is much larger than that in the nanoprisms. Higher annealing temperatures or a longer annealing time is needed for these nonsingle-crystal nanospheres to form a single crystal. In the following discussion, we consider all of the nanospheres as nearly single-crystal nanoparticles.

Figure 2a is a dark-field TEM image of a single nanoprism in high magnification where the polycrystalline structure of the nanoparticle is very clear. In Figure 2b, the well-observed thickness fringes indicate that the thermally annealed nanoparticle is a single grain. The polycrystalline structure of the nanoprism is further confirmed by the ring structure in the

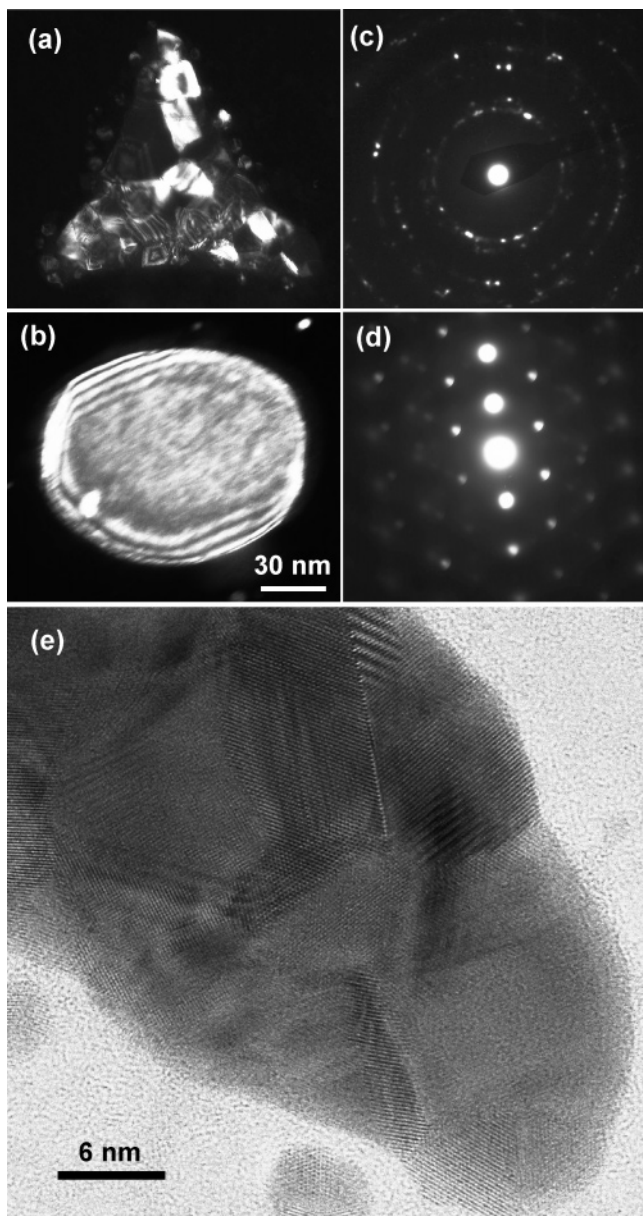


Figure 2. (a and b) Dark-field TEM images of a gold nanoprisim and a nanosphere, respectively. The different contrast in the dark-field image (a) indicates that the as-deposited gold nanoparticle is polycrystalline. The well-observed thickness fringes in the dark-field image of the nanosphere indicate that the thermally annealed particle is a single grain. The polycrystalline nanoprisim and single-crystalline nanosphere structures can be further confirmed by their selected-area electron diffraction patterns (c and d, respectively). (e) High-resolution TEM image of one tip of an as-deposited nanoprisim, which clearly shows that the prismatic gold nanoparticles are polycrystalline with many lattice defect structures, such as twin boundaries and stacking faults.

selected-area electron diffraction (SAED) pattern as shown in Figure 2c. The bright spots in the SAED pattern indicate there are some larger crystal grains within the nanoprisim. The SAED pattern of a thermally annealed nanosphere is shown in Figure 2d, which reveals that most of the defect structures present in the prismatic nanoparticles have been eliminated and the nanosphere has a nearly single-crystalline structure. Figure 2e is a high-resolution TEM image of the tip of one nanoprisim before annealing, which clearly shows all kinds of defects present among different grains of the nanoparticle, such as twin boundaries and stacking faults. Because of the great difference in crystal structure between the as-deposited prismatic and the

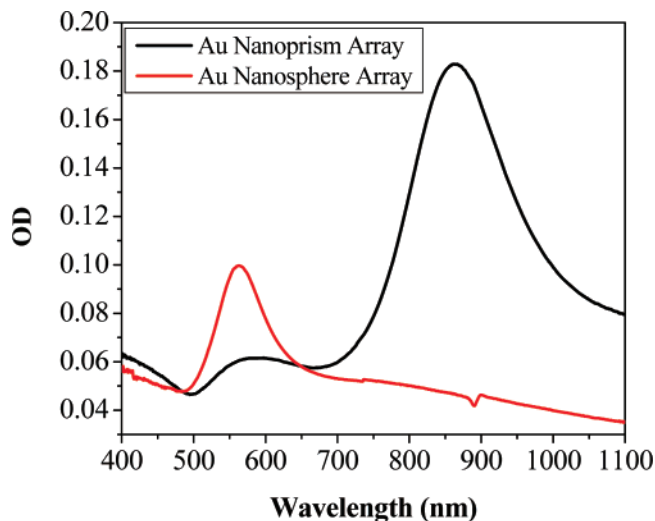


Figure 3. Absorption spectra of gold nanoprisim and nanosphere arrays. The absorption at the femtosecond pump pulse wavelength (400 nm) is very close for both samples.

thermally annealed spherical nanoparticles, they are ideal systems to study the effect of lattice crystallinity on the electron–phonon relaxation dynamics in gold nanoparticles.

B. Optical Transient Spectroscopy and Electron Phonon Dynamics. Before we carried out the femtosecond pump–probe experiment, we checked the extinction spectra of the nanoprisim and nanosphere arrays to find the difference in their pump efficiency at 400 nm. The extinction spectra of the gold nanoprisim and nanosphere arrays are shown in Figure 3, which indicate that the extinction intensity of the nanoprisim array at 400 nm is $\sim 10\%$ higher than that of the nanosphere array. The UV–vis spectra usually measure extinction (absorption and scattering) of nanoparticles, but scattering usually has a large effect only at the dipole resonance of nanoparticles. The extinction of gold nanoparticles at 400 nm corresponds to the absorption of the electron interband transition from 5d to 6sp above the Fermi level. Therefore, scattering is unlikely to be large at a 400 nm pump wavelength. With the same femtosecond pump–pulse power, the energy absorbed by the electrons of the two kinds of nanoparticles is within 10%. This absorption difference at 400 nm is most likely due to the difference in the cross section of prismatic and spherical nanoparticles of the same amount of atoms. The bisector of the prismatic nanoparticle is around 100 nm, and the radius of the corresponding spherical nanoparticle is around 40 nm. The cross section of prismatic nanoparticles is 15% larger than that of spherical nanoparticles. The absorption intensity is particularly important for comparing the electron–phonon relaxation dynamics since more energy absorbed by electrons results in a longer electron–phonon relaxation time. The surface plasmon resonance maxima of the nanoprisim and nanosphere arrays are located at 860 and 560 nm as shown in Figure 3, respectively. The surface plasmon resonance extinction intensity of the nanoprisim array is three times stronger than that of the nanosphere array, even though both arrays have the same amount of gold atoms. The stronger surface plasmon absorption of nanoprisms than nanospheres indicates that the prismatic nanoparticle has a higher extinction efficiency than the spherical nanoparticle.^{41,42} The probe wavelength is kept near the extinction peak (850 nm for the nanoprisim array and 560 nm for the nanosphere array) to maximize the intensity of the femtosecond transient bleach signal.

Figures 4a and 4b are femtosecond transient bleach signals of the nanoprisim and nanosphere arrays, respectively, under

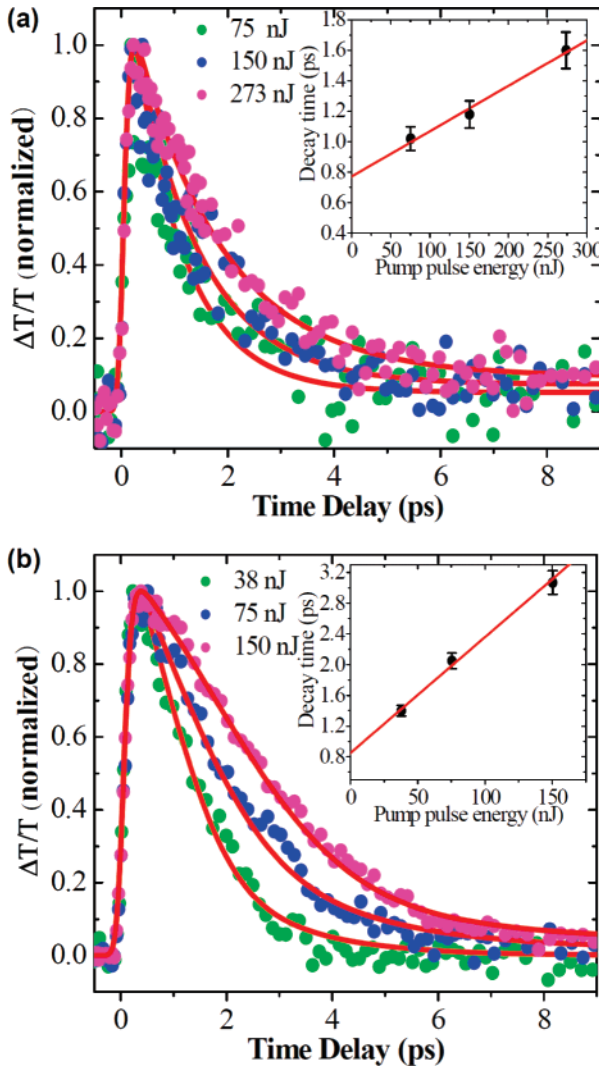


Figure 4. Normalized traces of pump power dependent transient bleach signals with the pump at 400 nm. The wavelengths of probe laser pulses are at (a) 850 nm for the prismatic gold nanoparticle array and (b) 560 nm for the spherical gold nanoparticle array. The inserts are linear fits of the relaxation time versus pump pulse energy.

different pump powers. The pump power dependent femtosecond transient bleach technique is a powerful method to measure the electron–phonon coupling constant, g . The coupling constant is calculated by fitting the power dependent electron–phonon relaxation time with a linear equation. The intercept of the linear equation corresponding to $\gamma T_0/g$,^{20,31} where T_0 is the ambient temperature and $\gamma = \pi^2 k_B^2 g(\epsilon_F)/3$ (k_B is Boltzmann’s constant, $g(\epsilon_F)$ is the electron density of states at the Fermi level), is $66 \text{ J m}^{-3} \text{ K}^{-2}$ for gold.⁴³ The inserts in Figure 4a,b are linear fits of the power dependent electron–phonon relaxation times of the nanoprisms and nanosphere arrays, respectively. From the intercepts of the linear equation, the electron–phonon coupling constant g for the nanoprisms and nanosphere are calculated to be $(2.2 \pm 0.3) \times 10^{16} \text{ W m}^{-3} \text{ K}^{-1}$ and $(2.6 \pm 0.5) \times 10^{16} \text{ W m}^{-3} \text{ K}^{-1}$, respectively. The two electron–phonon coupling constants are very close to the value observed for bulk gold,^{29,44} $(3.0 \pm 0.5) \times 10^{16} \text{ W m}^{-3} \text{ K}^{-1}$. This is due to the fact that the matrix elements involve one center term on the gold atoms.

Our experimental results show that the effect of crystalline structure (polycrystalline or nearly single crystalline) does not affect the electron–phonon coupling constant of the gold nanoparticles, but we do observe that there is a large difference in the relaxation dynamics of transient bleach signals between

the nanosphere and the nanoprisms arrays under the same laser pump pulse energy. With 75 nJ/pulse pump power, the electron–phonon relaxation time is $1.2 \pm 0.2 \text{ ps}$ for the gold nanoprisms and $2.1 \pm 0.3 \text{ ps}$ for the gold nanosphere. With 150 nJ/pulse pump power, the electron–phonon relaxation time is $1.6 \pm 0.3 \text{ ps}$ for the gold nanoprisms and $3.1 \pm 0.4 \text{ ps}$ for the gold nanosphere. The relaxation time of the gold spherical nanoparticles is nearly twice as large as that of prismatic nanoparticles under the same pump power. The difference in the electron–phonon relaxation time in the nearly single-crystalline and polycrystalline gold nanoparticles is demonstrated by the inserts of Figure 4. The linear fits of the two series experimental data give the same intercept but different slopes (0.015 for the nearly single-crystalline nanosphere, 0.003 for the polycrystalline nanoprisms).

We further considered the difference in the energy deposition within the two nanoparticle arrays. Since the energy deposited to the prismatic nanoparticle array is 10% more than that in the spherical one, the initial electron temperature in prismatic gold nanoparticles is thus higher than that in spherical gold nanoparticles under the same laser excitation intensity. If the nanosphere array absorbs 10% more energy, the excited electrons in nanospheres should reach the same temperature as those in nanoprisms. The electron–phonon relaxation time of nanospheres under this new laser excitation intensity can be calculated as the following. For low pump laser power, the electron–phonon relaxation time τ_{e-ph} is given by^{20,31}

$$\tau_{e-ph} = \gamma(T_0 + \Delta T)/g \quad (1)$$

where γ equals $66 \text{ J m}^{-3} \text{ K}^{-2}$, T_0 is the ambient temperature, ΔT is the increase of the electronic temperature induced by the energy deposited by the laser pulse, and g is the electron–phonon coupling constant. Since $\gamma T_0/g$ is given by the intercept of the linear fit of the power dependent electron–phonon coupling time ($\gamma T_0/g \approx 0.8 \text{ ps}$ from inserts of Figure 4), eq 1 can be reformatted as

$$\tau_{e-ph} = \gamma \Delta T/g + 0.8 \quad (2)$$

If gold nanospheres absorb 10% more energy, ΔT would be 10% larger and $(\tau_{e-ph} - 0.8)$ would also increase 10%. The electron–phonon relaxation time of the nanosphere array would be 2.2 ± 0.3 and $3.3 \pm 0.4 \text{ ps}$ for pump powers of 82.5 and 165 nJ/pulse, respectively. Now we can compare the electron–phonon relaxation time of the nanosphere array and the nanoprisms array under the same energy deposition. The electron–phonon relaxation times of the nanoprisms array are 1.2 ± 0.2 and $1.6 \pm 0.3 \text{ ps}$ for the pump power of 75 and 150 nJ, respectively. The difference of the electron–phonon relaxation time between the nanosphere and the nanoprisms is even larger for the same energy deposition by the pump laser pulse.

C. Grain Boundary Mechanism. The shorter relaxation time for prismatic gold nanoparticles compared with that for the spherical nanoparticles is a consequence of the difference in the internal crystalline structures. The prismatic gold nanoparticles are polycrystalline nanoparticles with many defects like grain boundaries as shown in the high-resolution TEM image (Figure 2e). The spherical gold nanoparticles have much fewer defects after the high-temperature annealing as shown in Figure 2b,d. The shorter relaxation time for prismatic gold nanoparticles than that for spherical nanoparticles could be due to the more effective inelastic scattering of electrons by these defects (the collisions of electrons with lattice imperfections). In single-crystal metal, the conductive electron collides with a phonon

within the mean free path of the electron (40–50 nm). From the high-resolution TEM image of polycrystalline gold nanoprisms, the averaged grain size is $\sim 13.3 \pm 3.1$ nm, which is much smaller than the mean free path of electrons in gold. In the nearly single-crystalline gold nanosphere, the grain size is very close to the size of the nanosphere (~ 80 nm). Therefore, the collision of electrons with grain boundaries happens more frequently than the electron–phonon collisions in the polycrystalline gold nanoprism.^{45,46} Among all kinds of crystal defects (e.g., dislocation, stacking fault, and grain boundary), grain boundaries are one of the most efficient structures for electron scattering. Reiss et al.⁴⁷ theoretically calculated the transmission probability of an electron through a single grain boundary in a polycrystalline metal film. They found the probability is close to 0.7 ± 0.1 . This probability means that $\sim 30\%$ of the electrons will be scattered (elastically or inelastically) when they try to pass through a grain boundary. Another way to interpret this probability is that each electron will be scattered once on average if it passes three grain boundaries. In the polycrystalline gold nanoprism, the hot electron collides with grain boundaries several times before it transfers the energy to the lattice through electron–phonon interaction. Part of these electron grain boundary collisions would be inelastic, and the electronic energy could be transferred to the defect sites. Therefore, the electron–grain boundary interaction could account for the observed shorter electron–phonon relaxation time of gold nanoprisms than that of gold nanospheres under the same energy deposition of the pump laser pulse.

The extra electron–grain boundary collisions in polycrystalline nanoprisms provide additional channels for the relaxation of hot electronic energy, which do not exist in single-crystalline nanospheres. Thus, the electronic energy relaxation in nanoprisms is faster than that in nanospheres. Furthermore, the extrapolations of liner fits to zero pump pulse energy shown in the inserts of Figure 4 are close to 0.8 ps. This indicates that at lower pump pulse energy, the effect of the electron–grain boundary interaction to the electronic energy relaxation in polycrystalline gold nanoprisms is very small, which leads to the similar electronic energy relaxation time in both of the polycrystalline and the single-crystalline gold nanoparticles. As the energy of the laser pump pulse increases, the hot electrons are pumped to higher temperatures, and the contribution from inelastic scattering with the grain boundaries to the electronic energy relaxation increases.

The grain boundary also explains the fact that the observed tails of transient bleach signals in nanoprisms are higher (~ 0.1) than that in nanospheres (close to zero) as shown in Figure 4. This is due to the slower phonon–phonon relaxation in polycrystalline nanoprisms compared to that in single-crystalline nanospheres. This could be due to the fact that phonons in nanoprisms are highly localized because of the grain boundary and thus remain in the nanoparticle lattice longer, while phonons in single-crystalline spherical nanoparticles have a longer coherent distance that could transfer their thermal energy to the environment faster. Therefore, the tails of the transient bleach signals of single-crystalline nanospheres are lower and almost around zero.

An alternative explanation of the difference in the rate of electron–phonon relaxation is the difference in the phonon density and phonon frequencies in the two lattices. We have previously measured that the symmetric coherent phonon vibration period in the prismatic nanoparticle was 74 ps while it is 27 ps in the spherical nanoparticle.⁴⁸ This means that the phonon frequency in the spherical nanoparticle is almost three

times larger than that in the prism. The exact density of the phonon states for different frequencies that can couple with the electrons will determine the relaxation rates. Since the frequencies of the phonon are different in the two lattices, the density of states and thus the rates of energy transfer will undoubtedly be different. For real amorphous solids, there are no phonons, but rather highly localized, high density, and high frequency (molecular type) vibrations. The selection rules governing the transfer of momentum or energy from the electron to these vibrations are not as restrictive as those governing the transfer to the phonons. As a result, the electron–lattice relaxation in the disordered prism is expected to be faster than that in the more crystalline lattice.

Acknowledgment. The authors thank Mr. Christopher Tabor for his careful reading of the manuscript. This work is supported by the Division of Material Research of the National Science Foundation (Grant 0138391).

References and Notes

- Quinten, M.; Leitner, A.; Krenn, J. R.; Aussenegg, F. R. *Opt. Lett.* **1998**, *23*, 1331–1333.
- Schuck, P. J.; Fromm, D. P.; Sundaramurthy, A.; Kino, G. S.; Moerner, W. E. *Phys. Rev. Lett.* **2005**, *94*, 017402.
- Maier, S. A.; Kik, P. G.; Atwater, H. A.; Meltzer, S.; Harel, E.; Koel, B. E.; Requicha, A. A. G. *Nat. Mater.* **2003**, 229–232.
- Haes, A. J.; Hall, W. P.; Chang, L.; Klein, W. L.; Van Duyne, R. P. *Nano Lett.* **2004**, *4*, 1029–1034.
- Haes, A. J.; Chang, L.; Klein, W. L.; Van Duyne, R. P. *J. Am. Chem. Soc.* **2005**, *127*, 2264–2271.
- Elghanian, R.; Storhoff, J. J.; Mucic, R. C.; Letsinger, R. L.; Mirkin, C. A. *Science* **1997**, *277*, 1078–1081.
- Loo, C.; Lowery, A.; Halas, N.; West, J.; Drezek, R. *Nano Lett.* **2005**, *5*, 709–711.
- Huang, X. H.; El-Sayed, I. H.; Qian, W.; El-Sayed, M. A. *J. Am. Chem. Soc.* **2006**, *128*, 2115–2120.
- Huang, W. Y.; Qian, W.; El-Sayed, M. A. *J. Appl. Phys.* **2005**, *98*, 114301.
- Wang, Z. L.; Petroski, J. M.; Green, T. C.; El-Sayed, M. A. *J. Phys. Chem. B* **1998**, *102*, 6145–6151.
- El-Sayed, M. A. *Acc. Chem. Res.* **2001**, *34*, 257–264.
- Hartland, G. V. *Annu. Rev. Phys. Chem.* **2006**, *57*, 403–430.
- Huang, W. Y.; Qian, W.; El-Sayed, M. A. *Nano Lett.* **2004**, *4*, 1741–1747.
- Zhang, J. Z. *Acc. Chem. Res.* **1997**, *30*, 423–429.
- Link, S.; El-Sayed, M. A. *J. Phys. Chem. B* **1999**, *103*, 8410–8426.
- Link, S.; El-Sayed, M. A. *Int. Rev. Phys. Chem.* **2000**, *19*, 409–453.
- Voisin, C.; Del Fatti, N.; Christofilos, D.; Vallee, F. *J. Phys. Chem. B* **2001**, *105*, 2264–2280.
- Link, S.; El-Sayed, M. A. *Annu. Rev. Phys. Chem.* **2003**, *54*, 331–366.
- Lee, P. A.; Ramakrishnan, T. V. *Rev. Mod. Phys.* **1985**, *57*, 287–337.
- Hodak, J.; Martini, I.; Hartland, G. V. *Chem. Phys. Lett.* **1998**, *284*, 135–141.
- Ahmadi, T. S.; Logunov, S. L.; El-Sayed, M. A. *J. Phys. Chem.* **1996**, *100*, 8053–8056.
- Logunov, S. L.; Ahmadi, T. S.; El-Sayed, M. A.; Khoury, J. T.; Whetten, R. L. *J. Phys. Chem. B* **1997**, *101*, 3713–3719.
- Link, S.; Burda, C.; Mohamed, M. B.; Nikoobakht, B.; El-Sayed, M. A. *Phys. Rev. B* **2000**, *61*, 6086–6090.
- Hodak, J. H.; Henglein, A.; Hartland, G. V. *J. Chem. Phys.* **1999**, *111*, 8613–8621.
- Del Fatti, N.; Flytzanis, C.; Vallee, F. *Appl. Phys. B* **1999**, *68*, 433–437.
- Arbouet, A.; Voisin, C.; Christofilos, D.; Langot, P.; Del Fatti, N.; Vallee, F.; Lerne, J.; Celep, G.; Cottancin, E.; Gaudry, M.; Pellarin, M.; Broyer, M.; Maillard, M.; Pileni, M. P.; Treguer, M. *Phys. Rev. Lett.* **2003**, *90*, 177401.
- Sun, C. K.; Vallee, F.; Acioli, L. H.; Ippen, E. P.; Fujimoto, J. G. *Phys. Rev. B* **1994**, *50*, 15337–15348.
- Roberti, T. W.; Smith, B. A.; Zhang, J. Z. *J. Chem. Phys.* **1995**, *102*, 3860–3866.
- Groeneveld, R. H. M.; Sprik, R.; Legendijk, A. *Phys. Rev. B* **1995**, *51*, 11433–11445.

- (30) Link, S.; Burda, C.; Wang, Z. L.; El-Sayed, M. A. *J. Chem. Phys.* **1999**, *111*, 1255–1264.
- (31) Hodak, J. H.; Martini, I.; Hartland, G. V. *J. Phys. Chem. B* **1998**, *102*, 6958–6967.
- (32) Hodak, J. H.; Henglein, A.; Hartland, G. V. *J. Chem. Phys.* **2000**, *112*, 5942–5947.
- (33) Nisoli, M.; Stagira, S.; DeSilvestri, S.; Stella, A.; Tognini, P.; Cheyssac, P.; Kofman, R. *Phys. Rev. Lett.* **1997**, *78*, 3575–3578.
- (34) Halte, V.; Bigot, J. Y.; Palpant, B.; Broyer, M.; Prevel, B.; Perez, A. *Appl. Phys. Lett.* **1999**, *75*, 3799–3801.
- (35) Darugar, Q.; Qian, W.; El-Sayed, M. A.; Pileni, M. P. *J. Phys. Chem. B* **2006**, *110*, 143–149.
- (36) Wang, X. D.; Summers, C. J.; Wang, Z. L. *Nano Lett.* **2004**, *4*, 423–426.
- (37) Kosiorek, A.; Kandulski, W.; Chudzinski, P.; Kempa, K.; Giersig, M. *Nano Lett.* **2004**, *4*, 1359–1363.
- (38) Huang, W.; Qian, W.; El-Sayed, M. A. *J. Am. Chem. Soc.* **2006**, *128*, 13330–13331.
- (39) Logunov, S. L.; Volkov, V. V.; Braun, M.; El-Sayed, M. A. *Proc. Natl. Acad. Sci. U.S.A.* **2001**, *98*, 8475–8479.
- (40) Huang, W. Y.; Qian, W.; El-Sayed, M. A. *J. Phys. Chem. B* **2005**, *109*, 18881–18888.
- (41) Jensen, T. R.; Schatz, G. C.; Van Duyne, R. P. *J. Phys. Chem. B* **1999**, *103*, 2394–2401.
- (42) Jain, P. K.; Lee, K. S.; El-Sayed, I. H.; El-Sayed, M. A. *J. Phys. Chem. B* **2006**, *110*, 7238–7248.
- (43) Ashcroft, N. W.; Mermin, N. D. *Solid State Physics*; Holt, Rinehart & Winston: New York, 1976.
- (44) Groeneveld, R. H. M.; Sprik, R.; Lagendijk, A. *Phys. Rev. Lett.* **1990**, *64*, 784–787.
- (45) Elsayedali, H. E.; Juhasz, T. *Phys. Rev. B* **1993**, *47*, 13599–13610.
- (46) Elsayedali, H. E.; Juhasz, T.; Smith, G. O.; Bron, W. E. *Phys. Rev. B* **1991**, *43*, 4488–4491.
- (47) Reiss, G.; Vancea, J.; Hoffmann, H. *Phys. Rev. Lett.* **1986**, *56*, 2100–2103.
- (48) Huang, W.; Qian, W.; El-Sayed, M. A. *Proc. SPIE-Int. Soc. Opt. Eng.* **2005**, 5927, 592701.